UCLA

UCLA Previously Published Works

Title

Three-Dimensional Ultrastructure of the Normal Rod Photoreceptor Synapse and Degenerative Changes Induced by Retinal Detachment.

Permalink

https://escholarship.org/uc/item/7dv2568n

Journal

Journal of Neuroscience, 43(30)

Authors

Torten, Gil

Fisher, Steven

Linberg, Kenneth

et al.

Publication Date

2023-07-26

DOI

10.1523/JNEUROSCI.2267-22.2023

Peer reviewed

Cellular/Molecular

Three-Dimensional Ultrastructure of the Normal Rod Photoreceptor Synapse and Degenerative Changes Induced by Retinal Detachment

Gil Torten,[1]* Steven K. Fisher,[2,3]* Kenneth A. Linberg,[2] Gabriel Luna,[2] Guy Perkins,[4] Mark H. Ellisman,[4] and David S. Williams[1,5,6]

[1]Departments of Ophthalmology and Neurobiology, Stein Eye Institute, David Geffen School of Medicine, University of California, Los Angeles, Los Angeles, California 90095, [2]Neuroscience Research Institute, University of California, Santa Barbara, Santa Barbara, California 93117, [3]Molecular, Cellular, and Developmental Biology, University of California, Santa Barbara, Santa Barbara, California 93117, [4]National Center for Microscopy and Imaging Research and Department of Neurosciences, University of California, San Diego, La Jolla, California 92093, [5]Molecular Biology Institute, University of California, Los Angeles, Los Angeles, California 90095, and [6]Brain Research Institute, David Geffen School of Medicine, University of California, Los Angeles, Los Angeles, California 90095

The rod photoreceptor synapse is the first synapse of dim-light vision and one of the most complex in the mammalian CNS. The components of its unique structure, a presynaptic ribbon and a single synaptic invagination enclosing several postsynaptic processes, have been identified, but disagreements about their organization remain. Here, we have used EM tomography to generate high-resolution images of 3-D volumes of the rod synapse from the female domestic cat. We have resolved the synaptic ribbon as a single structure, with a single arciform density, indicating the presence of one long site of transmitter release. The organization of the postsynaptic processes, which has been difficult to resolve with past methods, appears as a tetrad arrangement of two horizontal cell and two rod bipolar cell processes. Retinal detachment severely disrupts this organization. After 7 d, EM tomography reveals withdrawal of rod bipolar dendrites from most spherules; fragmentation of synaptic ribbons, which lose their tight association with the presynaptic membrane; and loss of the highly branched telodendria of the horizontal cell axon terminals. After detachment, the hilus, the opening through which postsynaptic processes enter the invagination, enlarges, exposing the normally sequestered environment within the invagination to the extracellular space of the outer plexiform layer. Our use of EM tomography provides the most accurate description to date of the complex rod synapse and details changes it undergoes during outer segment degeneration. These changes would be expected to disrupt the flow of information in the rod pathway.

Key words: electron microscope tomography; photoreceptor; retinal detachment; rod degeneration; rod spherule; synapse

---

Significance Statement

Ribbon-type synapses transmit the first electrical signals of vision and hearing. Despite their crucial role in sensory physiology, the three-dimensional ultrastructure of these synapses, especially the complex organization of the rod photoreceptor synapse, is not well understood. We used EM tomography to obtain 3-D imaging at nanoscale resolution to help resolve the organization of rod synapses in normal and detached retinas. This approach has enabled us to show that in the normal retina a single ribbon and arciform density oppose a tetrad of postsynaptic processes. In addition, it enabled us to provide a 3-D perspective of the ultrastructural changes that occur in response to retinal detachment.

Introduction

Rod photoreceptor cells are highly sensitive light receptors that operate in dim light (i.e., scotopic vision). The synaptic terminal [rod spherule (RS)] of these cells is one of the most complex synapses in the mammalian CNS. It is uniquely structured to couple the high sensitivity of the rod cell with high temporal resolution of changes in the lighting environment (Rodieck, 1998). Rapid modulation of neurotransmitter release and rapid responses by its postsynaptic cells result from the presence of a presynaptic ribbon, molecular machinery that rapidly and precisely conveys synaptic vesicles to a presynaptic release site (Matthews and Sterling, 2008; LoGiudice and Matthews, 2009; Zampighi et al., 2011), and the presence of a synaptic invagination that encloses the postsynaptic processes within a tight, sequestered environment. The latter assures the ability of the cell to rapidly regulate glutamate concentration in the extracellular space (Sterling et al., 1987; Rao-Mirotznik et al., 1995; Rodieck, 1998).

The ultrastructure of rod synapses has been the focus of dozens of studies since the first by Sjöstrand (1958). The first comprehensive description was by Missotten (1965), where he described two or three type 1 and 2 postsynaptic processes within the synaptic invagination (Fig. 1). These are now known to be rod bipolar (RB; Fig. 1, first type) dendrites and horizontal cell axon terminals (HCATs; Fig. 1, second type). The former transmits signals through the visual pathway ultimately to the ganglion cells, whose axons make up the optic nerve, whereas the latter integrates signals laterally across photoreceptors (Zampighi et al., 2011).

Although there is general agreement about RS structure, controversies remain about important details, such as the number and organization of the postsynaptic processes as well as the synaptic ribbon and arciform density. Accurate definitions of these features have implications for the flow of visual information through retinal pathways (Rodieck, 1998). The lack of agreement has arisen largely because of limitations for describing the 3-D ultrastructure of such a complex structure. Even serial section EM reconstruction (Missotten, 1965; Grünert and Martin, 1991; Rao-Mirotznik et al., 1995; Migdale et al., 2003) lacks sufficient z-axis resolution (~80–90 nm in past studies) to accurately define RS 3-D structure.

We used the high-resolution imaging capabilities of EM tomography to study the 3-D ultrastructure of the RS and changes it undergoes after retinal detachment. This approach allowed us to create high-resolution 3-D models (Kremer et al., 1996; Burette et al., 2012; Phan et al., 2017). It also reduces the number of sections required to reconstruct the synaptic invagination and improves z-resolution to ~2–3 nm, thus revealing structural details with greater accuracy and precision.

Rhegmatogenous retinal detachment, in which there is a tear across the retina, is a relatively common cause of vision loss; it can occur by mechanical damage to the retina, in response to some inherited retinal diseases (Nash et al., 2021; Collin et al., 2022; Martin-Gutierrez et al., 2022), and in cultured retinal explants (Kung et al., 2017). Although retinal reattachment surgery can reverse outer segment degeneration, significant visual deficits often remain (Sørensen et al., 2020). Previous EM studies have shown dramatic remodeling of the RS in response to detachment (Erickson et al., 1983; Linberg et al., 2009) including changes in its shape, retraction from the outer plexiform layer (OPL) (Townes-Anderson et al., 2021), and retraction of RB dendrites from the synaptic invagination (Linberg et al., 2006b). However, details requiring higher resolution are not understood; for example, although the HCAT endings tend to remain within the invagination, little is known about changes they may undergo.
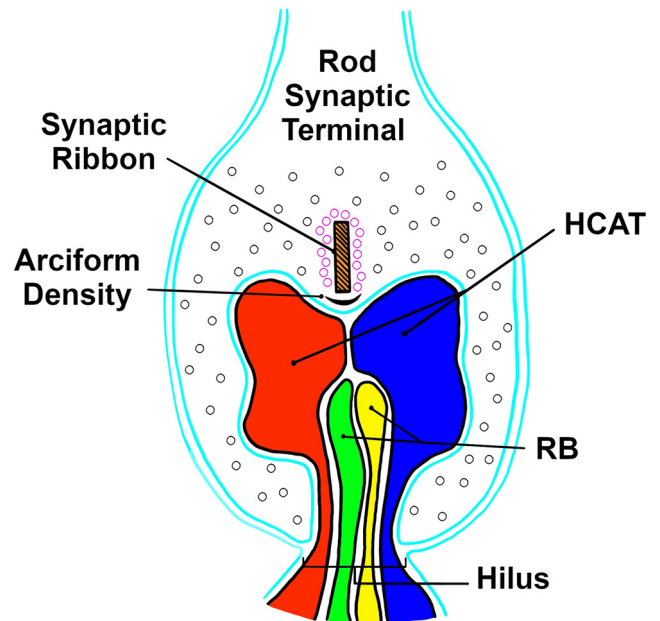

Figure 1. Diagram of the rod spherule, showing the organization originally illustrated by Missotten (1965). In Missotten's description the synaptic ribbon was referred to as a "lamella", the RBs as the "first type terminal buds", and the HCATs as the "second type terminal buds".

Because of the precise regulation of glutamate release within the RS, it is likely that even modest structural remodeling of its invagination would have significant effects on neurotransmission to its postsynaptic neurons (Sørensen et al., 2020). Here, we describe changes in the RS and their postsynaptic processes after the first week of cellular remodeling induced by detachment.

Materials and Methods

EM tomography. All tissue used in this study was generated from female domestic cats, *Felis catus*, in a previous conventional EM study (Erickson et al., 1983), which describes the tissue preparation in detail. Briefly, following intracardiac perfusion with 1% glutaraldehyde and 1% formaldehyde in phosphate buffer, pH 7.1, eyes were enucleated, kept in the same aldehyde fixative overnight, postfixed for 1 h in 2% osmium tetroxide in phosphate buffer, dehydrated in an ethanol series, and embedded in Araldite. For the rhegmatogenous retinal detachment studies, the detachment surgery had been performed in one eye of each fully anesthetized animal 7 d before tissue fixation. As described in detail by the original study (Erickson et al., 1983), a small hole was made in the superior retina, through which 0.5% aqueous Healon (sodium hyaluronate) was injected into the subretinal space, thus creating a retinal detachment that radiated outward from the retinal hole toward the optic disk. Healon ensures that the retina stays detached for the duration of the experiment. Control retinas were prepared from animals that were not used in the detachment experiments. All animals had been maintained on a 12 h light/dark cycle and were killed midmorning.

Samples imaged at University of California, San Diego (UCSD) were sectioned at 400–500 nm, whereas samples imaged at University of California, Los Angeles (UCLA) were sectioned at 200 nm serially (four serial sections per tomogram); both were then counterstained with uranyl acetate followed by lead citrate. Colloidal gold particles (15 nm) were added to both sides of each section for fiducial alignment, and the sections were imaged on a custom JEOL JEM-4000EX IVEM using a specially constructed charge-coupled device camera with a pixel array of 1960 × 2560 (UCSD) or a JEOL JEM-1400Plus (UCLA). The tilt series was acquired either manually (single-axis tomograms, −60° –60°, 1° increments; UCSD) or automatically through the program SerialEM (dual-axis tomograms, −65° to 65°, 1.5° increments; UCSD). The specimens were irradiated with electrons for ~20 min to limit

Table 1. List of tomograms from which figures were generated

Condition	Name of tomogram	Figure(s)	Number of sections	Section thickness	Pixel size (nm)	Location of image acquisition
Control	nCat414_01	10	1	400–500 nm	2.08	UCSD
	nCat414_02	2, 4, 10	1	400–500 nm	2.86	UCSD
	nCat414_03	3, 5, 7, 9, 10	1	400–500 nm	2.08	UCSD
	nCat414_04	11	1	400–500 nm	2.60	UCSD
	nCat414_12	7, 9	1	400–500 nm	2.08	UCSD
	nCat414_16	7	1	400–500 nm	1.30	UCSD
	nCat414_021621	6, 9, 10, 11	4	200 nm	0.847	UCLA
	nCat414_031121	8, 10	4	200 nm	1.34	UCLA
	nCat414_102021	6	4	200 nm	0.847	UCLA
7d RD	7drd5	9	1	400–500 nm	2.21	UCSD
	7drd9	2, 4, 5, 9, 11	1	400–500 nm	2.42	UCSD
	7drd10	3, 5, 10	1	400–500 nm	2.42	UCSD
	7drd12	4, 11	1	400–500 nm	1.04	UCSD
	7drd14	9	1	400–500 nm	1.04	UCSD

anisotropic specimen thinning during image collection before initiating a tilt series. During data collection, the illumination was held to near-parallel beam conditions, and the beam intensity was kept constant.

Tomograms were reconstructed, serial tomograms were joined, and 3-D models were generated using the software IMOD3D. Tomogram alignment and reconstruction were done in etomo, following the IMOD guide on the associated University of Colorado website (https://bio3d. colorado.edu/imod/doc/etomoTutorial.html). Briefly, image alignment was done using fiducial models based on added colloidal gold for both tilt axes. Dual-axis tomograms taken at UCLA were combined, and serial tomograms were stacked using etomo as well.

We used z-slice thickness to estimate z-axis resolution. The z-slice thickness was obtained from the total number of z-slices divided by the total depth of each tomogram. Within the presented tomograms, the number of z-slices ranged from 140 to 714, and the depth of the tomogram volume was either 800 nm (4 serial 200 nm tomograms at UCLA) or 400–500 nm (at UCSD), leading to a z-resolution of ~2 nm (1.8 ± 0.1, mean ± SEM, $n = 14$). Segmentation of the tomograms was done by manually tracing contours for individual structural features using the IMOD drawing tools menu. In general, contours were traced on every three z-slices through the depth of the structure, although in some instances every z-slice was used. For scattered objects, the diameter was set in the object menu of IMOD. Each object was described as a closed or scattered (for vesicles) structure and assigned a specific color. Three-dimensional models were created using the mesh feature in IMOD, and in some cases the models were smoothed using the smoothsurf algorithm. Further image analysis was done in ImageJ for quantification of key structures.

During segmentation, HCATs were identified by the presence of intracellular vesicles of a larger size (~45 nm) than standard cytoplasmic synaptic vesicles. In control retinas, HCATs were also identified through their branching structure, and the extensive telodendria that extended from the main body of the process. RBs were identified by a lack of intracellular vesicles and membrane densification on the side of the RS membrane, apposed to the RB process. In detachment, these characteristics were maintained such that identification of these processes was straightforward in all but two cases; any processes lacking in both membrane densification and intracellular vesicles (see Fig. 9) were colored in cyan and are labeled with an asterisk in the figures. Previous conventional EM studies of this tissue by some of us (Linberg et al., 2009) indicated that the same criteria used to identify postsynaptic processes in the normal retina are valid in the detached retina.

Semithin sections of cat retinas were stained with Toluidine blue for 45 s before mounting with Permount (Thermo Fisher Scientific) and imaging with a Zeiss Axiophot microscope.

Statistical analyses. We performed quantification and analysis on 15 normal retina tomograms and 7 detached retina tomograms. Many tomograms contained two to three synapses, so in total, we analyzed 33 RSs (Table 1). In IMOD, the perimeter of the invaginating RS membrane

was traced with the freehand selections tool, and values were measured within IMOD. In tomograms containing a hilus, the shape was closed with a straight line directly through the hilus. For quantification of area, perimeter, circularity, and solidity (see below for equations), the relative center of the invagination, in terms of z-depth, was selected to include most of the postsynaptic processes and branching complexity. These measurements were made using ImageJ software. To measure ribbon length, three points were taken, one at either end of the ribbon and one in the central point of the ribbon along its length. Lines were generated from each of the two end points to the center point, and the lengths of the two lines were summed. Although it is difficult to obtain a highly accurate measurement of length because of the variable 3-D structure of the ribbon, using two separate lines allows for reasonable quantification of straight, as well as heavily arced, ribbons. Synaptic vesicle density for each spherule (as well as the proportions of vesicle types in the detached condition for each spherule) was measured by counting the vesicles within a volume that included 20 consecutive z-slices, 200 × 200 nm in area, situated within 150 nm from the invagination in X-Y, and near the relative center of the invagination in z. To separate out vesicle types in the detached condition, vesicle diameters were binned from 20 to 35 nm (normal), 35.1 to 45 nm (medium), and >45 nm (large). Ribbon, HCAT, RB, and mitochondria quantities were counted across the entire z-stack. The coefficient of variability of intervesicular distance along the ribbon was determined. First, the distance between adjacent vesicles was independently measured for each condition, along each individual ribbon, using an ImageJ plug-in designed in house. This plug-in allows the user to select the center of consecutive vesicles along each ribbon, and then it automatically measures the distance between these points on each side of each ribbon. Then, the mean and SDs of these values were calculated, and the SD was divided by the mean for each individual ribbon.

In cases where the hilus was present but not fully captured (a common result in detachment), a relative diameter was assigned by assuming that the visible portion of the hilus would continue in an elliptical shape beyond the borders of the tomogram. If not enough of the hilus was present to make this estimate, then it was omitted from the quantification. In cases where the invagination was simplified to indentations during detachment, the hilus was measured as the distance across the area contacted by the postsynaptic processes. The diameter of the hilus neck was determined by measuring the narrowest region between the hilus and the main body of the invagination.

All measurements were taken manually, and the analyses were done blinded with respect to identification of the experimental groups; although, the extent of degeneration in the detached condition made it obvious whether a given tomogram was from a detached or normal retina. Significance was calculated first by performing a Kolmogorov–Smirnov test to ensure normality. Normally distributed datasets were analyzed with two-tailed Student's t tests, and non-normally distributed datasets (specifically #HC, #RB, #Ribbons, and #Mitochondria) were analyzed with the Mann Whitney U test. All analyses were done in Prism (GraphPad).
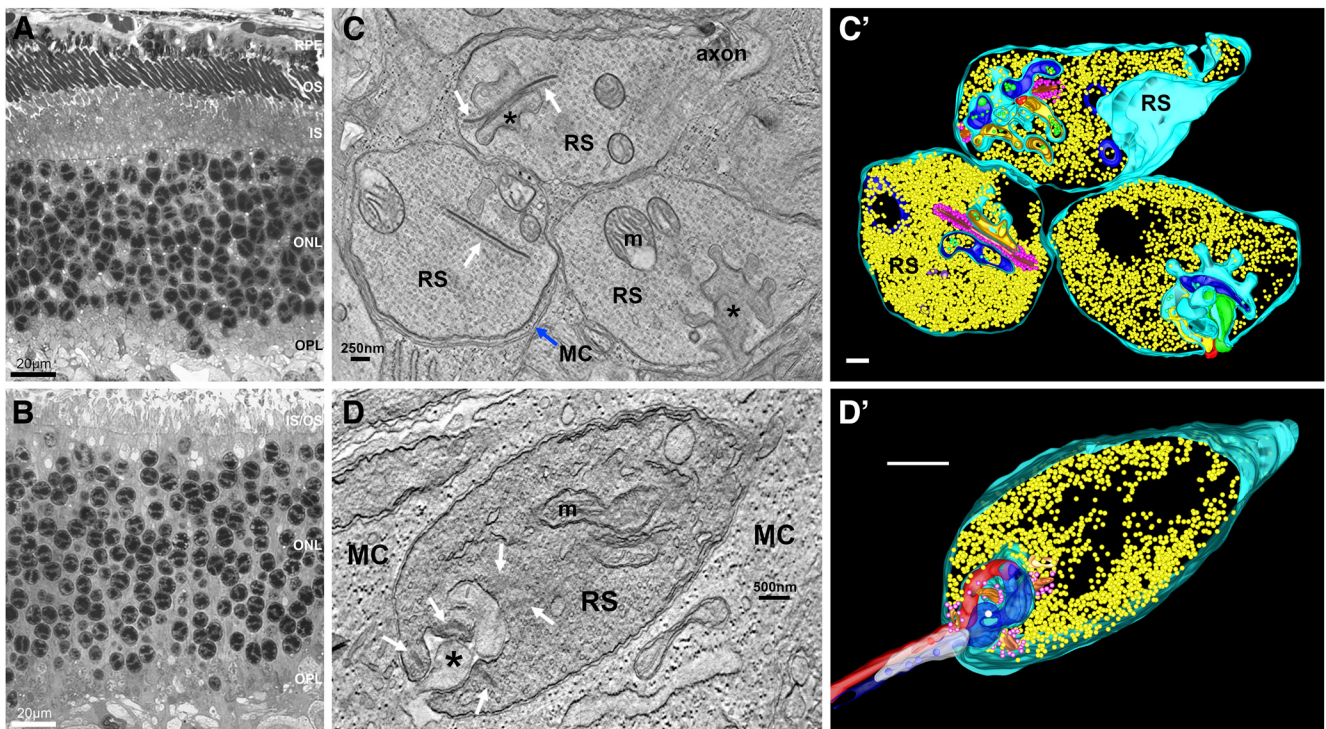
Figure 2. **A–D**, Overview of axonal R1-type rod spherules in normal (**A**, **C**) and 7 d detached (**B**, **D**) cat retina. Toluidine blue stained semithin section showing the photoreceptor layer in a control retina (**A**) as it interfaces with the RPE. OPL, outer plexiform layer. ONL, outer nuclear layer. IS, photoreceptor inner segments. OS, outer segments. RPE, retinal pigment epithelium. **B**, Toluidine blue–stained semithin section showing the photoreceptor layer in a retina that has been detached for 7 d. Note the disruption in outer segment structure, the misorganized photoreceptor nuclei, and the lack of an associated RPE/Choroid. **C**, A single z-slice showing three adjacent RSs. The terminals are filled with synaptic vesicles, synaptic ribbons (white arrows) surrounded by their own population of synaptic vesicles, and postsynaptic processes (asterisk) in two. Several mitochondria (m) are present. The RS are surrounded by thin MC (Müller cell) processes (blue arrow). **C'**, Three-dimensional model derived from the tomogram in **C**. Spaces lacking vesicles are because of the presence of (unsegmented) mitochondria. **D**, A single z-slice from a tomogram of an RS from detached retina, with an elongated shape characteristic of degenerating R1 terminals. A simplified invagination is present with swollen HCATs (asterisk) surrounded by expanded extracellular space. Five separate synaptic ribbons occur around the invagination (white arrows), although only one of the four (bottom right arrow) is distinctly visible in this z-slice. Also present are two distorted mitochondria and a population of synaptic vesicles. The RS is surrounded by greatly expanded MC processes. **D'**, Three-dimensional model derived from the tomogram in **D** showing the presence of free synaptic vesicles, five shortened ribbons each with a population of surrounding vesicles (magenta spheres), and two truncated postsynaptic processes (red and blue). Scale bars: **A**, **B**, 20 μm; **C**, **C'**, 250 nm; **D**, **D'**, 500 nm.

$$Circularity = \frac{4\pi(Area)}{(Perimeter)^2}$$

$$Solidity = \frac{Total\ Area}{Convex\ Area}.$$

Results

General features, normal and 7 d detached retina (Figs. 2, 3)
There are multiple layers of RSs across the top two-thirds of the OPL in the rod-dominated feline retina. Figure 2A shows the photoreceptor layer in the normal feline retina used as the control in our study, Figure 2B shows this same layer in a retina detached for 7 d (Table 2). The vast majority of the RSs are referred to as type R1, which contain an axon (Li et al., 2016). A second type, referred to as R2 (Li et al., 2016), occurs when the rod cell body lies adjacent to the OPL, hence lacking an axon, so that the synaptic site is essentially incorporated into the basal region of the cell body. Although RSs may vary in shape, in agreement with Li et al. (2016), we observed common general characteristics; for example, both the R1 and R2 types contain a large population of free synaptic vesicles that nearly fill the synaptic cytoplasm (Figs. 2C', 3A', yellow spheres). Quantification of the tomograms indicates that synaptic vesicle density varies among RSs (across a threefold range). For example, compare the range of synaptic vesicle densities among the three different adjacent RSs in

Figure 2C', although all three are essentially the same size and reconstructed within the same tissue volume. Moreover, the RS model in Figure 3A' has even fewer synaptic vesicles, despite including more depth than those in Figure 2C' (234 vs 140 z-slices).

Consistent features among all normal RSs are the presence of synaptic ribbons (Fig. 2, white arrows), as well as mitochondria (Fig. 2C, m). The synaptic ribbon opposes the postsynaptic processes and is associated with its own population of synaptic vesicles (Fig. 2C', magenta spheres). The ribbon forms an arc, so in some single sections the ends of the arc can give the impression of two separate ribbons (Fig. 2C, top RS, two white arrows). Single sections also normally depict the ribbon as a rather narrow structure. However, in Figure 3A, the ribbon (R) has been cut en face, illustrating a broader structure, which was validated by 3-D reconstruction (Fig. 4A,B, bottom). Note that this en face view still shows adjacent synaptic vesicles and that the ribbon is not bounded by a membrane (Fig. 3A). Transmission to second-order neurons occurs within the synaptic invagination, a pouch-like basal indentation of the RS membrane that contains closely organized postsynaptic processes. The immediate opening of the invagination denotes the hilus (Fig. 3A,B, red arrows); the invagination then narrows to form a neck (Fig. 3A, cyan arrows) that opens into the main body of the invagination. RB dendrites and HCATs enter the invagination through the hilus and are each identifiable by their characteristic features. In normal conditions, there are two HCATs per RS (Figs. 2, 3, red and blue processes). They branch deep within the invagination and contain apparent
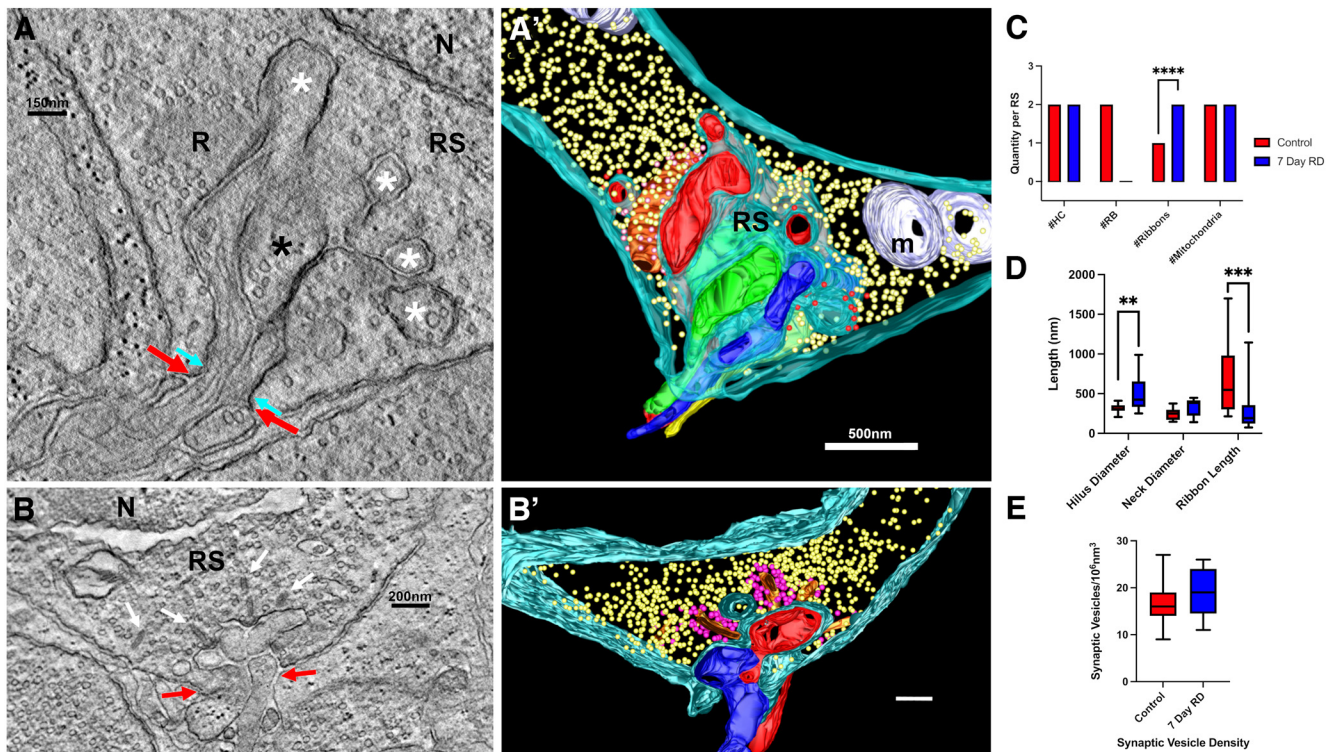
Figure 3. *A–B′*, Overview of perinuclear R2-type rod spherules in normal (*A, A′*) and 7 d detached (*B, B′*) cat retina. *A*, A *z*-slice from a tomogram of normal retina. Note small terminal endings of the HCAT (white asterisks). A finger of cytoplasm from the RS membrane itself, or a diverticulum (black asterisk), occurs within the invagination. The hilus, or opening into the invagination, is shown between red arrows. The neck, where the hilus shrinks to its minimal diameter, is shown between cyan arrows. The synaptic ribbon (R) is cut *en face*. N, Nucleus. *A′*, A 3-D model of the tomogram from *A*. *B*, A *z*-slice from a tomogram of a perinuclear RS from 7 d detached retina showing a shallow simplified invagination. There are four small synaptic ribbons (white arrows; *B*). The hilus is indicated by red arrows. *B′*, Three-dimensional model of the tomogram shows the presence of two HCATs (red and blue), free synaptic vesicles, and synaptic ribbons surrounded by their associated vesicles (magenta). *C*, Quantity of different key structures across healthy and 7 d detached retinas. The medians are depicted, and a Mann Whitney *U* test was used to determine the probability of no significant difference. *D*, Lengths (in nanometers) of key structures in healthy and detached retinas. Hilus and neck lengths were measured at the middle section of the hilus in terms of depth. *E*, Number of synaptic vesicles in the cytoplasm adjacent to the invagination in a 200 nm square across 20 *z*-slices in the relative center of the invagination in terms of depth through the tomogram. Each *z*-slice was ~2 nm thick; small variations in this thickness would be highly unlikely to affect vesicle counts by more than ~10% (1–2 vesicles), as the vesicle diameter (20–30 nm) makes up much of the volume depth. Mann Whitney *U* tests (*C*) and two-tailed Student's *t* tests (*D, E*) were used to determine the probability of no significant difference (see above, Materials and Methods for further statistical details); **$p < 0.005$, ***$p < 0.0005$, ****$p < 0.00005$. Scale bars: *A*, 150 nm; *A′*, 500 nm; *B, B′*, 200 nm.

Table 2. Color code for the 3-D models

Feature	Color
Rod spherule membrane	Cyan
Synaptic ribbon	Orange/gold
Mitochondria	Lavender
Cytoplasmic vesicles	Yellow
Ribbon-associated vesicles	Magenta
HCATs	Red and blue
RB dendrites	Green and yellow

synaptic vesicles (Fig. 2C', green spheres); their small branches are easily mistaken for multiple postsynaptic processes in single thin sections (Fig. 3A, white asterisk). In normal conditions, our data showed 2 RB dendrites per RS (Figs. 2, 3, green and yellow processes); however, they lack vesicles, and when RB dendrites lie adjacent to the RS membrane the membrane of the RS has an electron-dense coating (Vardi et al., 2000). This membrane densification is a quality that is used as a marker of sites opposed to mGluR6 receptors (Vardi et al., 2000; Migdale et al., 2003) and does not occur adjacent to the HCAT plasma membrane. In perinuclear synapses the invagination can dominate the volume of the cell basal cytoplasm (Fig. 3A). The invagination can also contain several profiles in individual sections that appear to be postsynaptic processes but instead are fingers of RS cytoplasm that extend into the invagination between postsynaptic processes

(Fig. 3A, asterisk). These extensions have been termed diverticuli previously (Rao-Mirotznik et al., 1995), the terminology that is used here.

In 7 d detached retinas, both types of RS were still found, with the type R1 axonal synapses remaining the vast majority. However, both RS types undergo significant structural and organizational changes. The R2 type RS becomes smaller and more angular (Fig. 3B) with a significantly simplified invagination. Rather than penetrating deep into the cytoplasm, the invagination may be missing almost entirely or, if present, is much simpler and shallower and can even become just a simple indent into the cell membrane (Fig. 4C,D). The R1 type RS often appeared in an elongated teardrop shape (Fig. 2D), with electron-dense cytoplasm and a somewhat ruffled plasma membrane. Some of these axonal RSs had retracted into the outer nuclear layer (ONL) or had degenerated entirely, and their reduced number was made evident by the presence of expanded Müller cell (MC) processes that filled in the space normally occupied by adjacent spherules (Fig. 2D). In the normal retina, these processes form only thin layers of cytoplasm surrounding the RS (Fig. 2C, MC, blue arrow). The R1 synaptic invagination, when present, had a very modified organization (Fig. 4C,D). Remaining RSs still contained mitochondria and a population of synaptic vesicles. Indeed, no significant difference in the density of the synaptic vesicles, within the cytoplasm near to the invagination, was
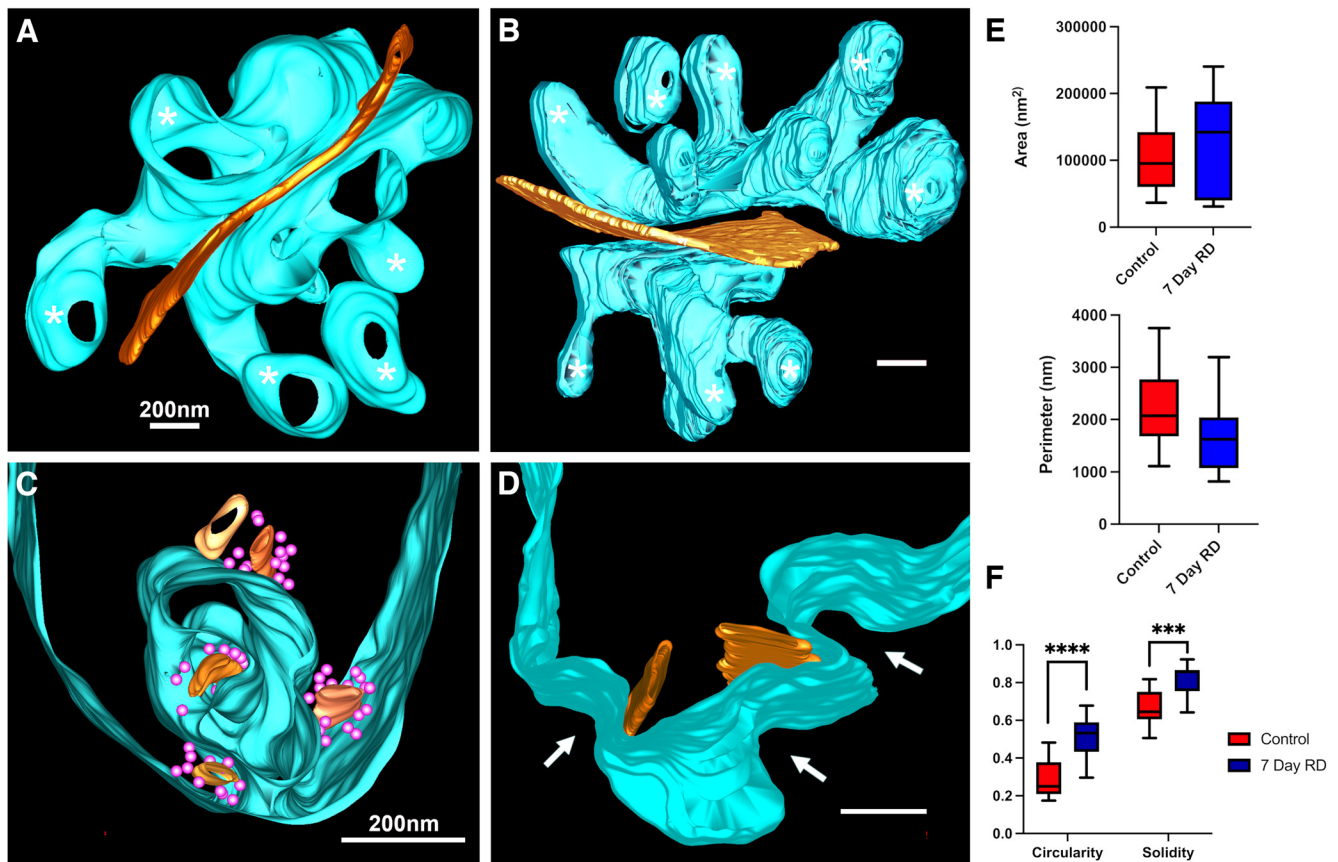
Figure 4. *A–D*, Organization of the synaptic invagination in normal (*A*, *B*) and detached (*C*, *D*) retinas. Three-dimensional models (*A*, *B*) of the synaptic invagination in two normal RSs, illustrating how the presynaptic membrane contours the endings of the postsynaptic processes, shown from the perspective of the rod axon. Synaptic ribbons (gold) lie between two lobes of the invagination that outline the terminal branches of the HCAT (asterisk). Models of two invaginations from 7 d detached retinas (*C*, *D*). In both cases, the deep branching of the invagination has been lost, resulting in extensive simplification. In *C* there are five independent synaptic ribbons (4 have a cloud of associated synaptic vesicles, magenta spheres), and in *D* there are two ribbons. In *D* there is no clearly definable invagination; instead, there are simple indentations of the plasma membrane (white arrows) opposite the postsynaptic processes (data not shown). *E*, Area and perimeter of the invaginating structure shown as box and whisker plots. For these measures, a section in the relative center of the invaginating structure was chosen, and the invaginating RS membrane was traced; the shape was closed by a straight line through the hilus if present. *F*, Circularity and solidity of the traced structure as drawn in *E*, shown as box and whisker plots. Student's *t* tests were used to determine the probability of no significant difference (see above, Materials and Methods for further statistical details); **p < 0.005, ***p < 0.0005, ****p < 0.00005. Scale bars: 200 nm.

detected between normal and 7 d detached retinas (Fig. 3*E*). In summary, after 7 d of detachment, the RS structure has undergone significant degeneration, with a simplified invagination (if it is present at all), an elongated teardrop shape, and retraction from the OPL as Müller cells expand to fill up the missing space. For the remainder of the present study, we built on these general features by analyzing models from EM tomograms of the RS at higher magnification.

The synaptic invagination and hilus, normal and 7 d detached retina (Figs. 4, 5)
First, we modeled the rod synaptic invagination and the hilus, which is the opening through which postsynaptic processes must pass. Despite classical illustrations of the synaptic invagination appearing as a round and smooth indentation of the RS basal membrane (Missotten, 1965; Fig. 1), its structural organization is in fact quite complex. The RS membrane contoured the endings of the HC processes almost perfectly such that viewing the RS membrane independently, as in Figure 4, *A* and *B*, provided an accurate indication of the location of these processes. Thus, each of the pockets created in the RS membrane (Fig. 4*A*,*B*, white asterisks, ~176 nM in diameter), reflects the smallest terminal branches of the HCAT telodendria, which appeared to be shaped

like lollipops. The synaptic ribbon (Fig. 4*A*,*B*, orange) was positioned in a deep bifurcating ridge formed by two lobes of the invagination.

The hilus opens at the base of the spherule (Fig. 5*A*), where it measured 314 ± 13 nm in diameter (*N* = 17, ±SEM; Fig. 3*D*). Slightly farther into the RS, it constricts slightly to form a neck (246 ± 16 nm in diameter, *N* = 17, ±SEM; Fig. 3*A*, cyan arrows, *D*), and then fully opens to the main volume of the invagination. When viewed from the perspective of the OPL (Fig. 5*A*), the diverticuli of the RS membrane were visible (Fig. 5*A*, asterisks). Figure 5*B* shows four postsynaptic processes at the hilus. The processes narrow as they pass through it (Fig. 3*A*). Within the invagination, the processes expand and fill the entire invagination. There was no apparent difference in the structure of the invagination or hilus in the R1- or R2-type terminals.

After a 7 d detachment, the complex infoldings of the invagination was almost completely lost (Fig. 4*C*,*D*). The bulbous outgrowths that surround the HCAT telodendria had disappeared, and the invagination had a much simplified shape. In Figure 4*C* the invagination remains but without its intricate infoldings. In Figure 4*D* the invagination is essentially absent, and the postsynaptic processes end in minor indentations along the base of the spherule (Fig. 4*D*, white arrows). Interestingly, we still observed
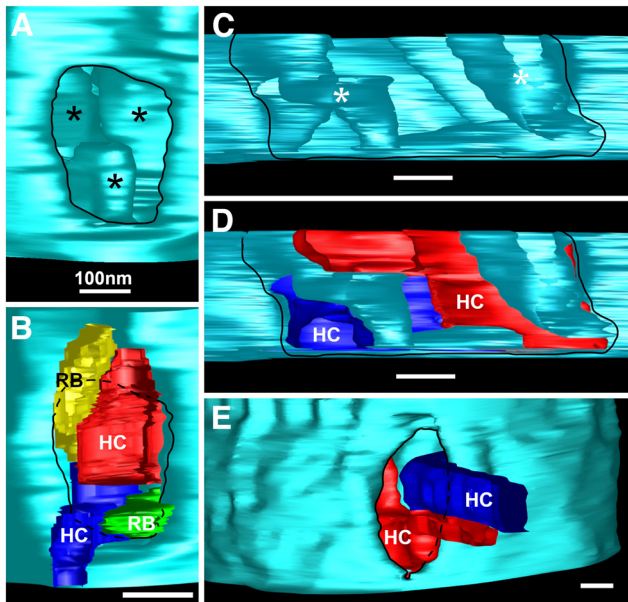
Figure 5. The hilus, the opening into the synaptic invagination, plays an important role in regulating the environment of the invagination and expands greatly during detachment. The perspective in each image is from the outer plexiform layer into the synaptic invagination. ***A, B,*** Model of the hilus (black outline; dashed line in ***B*** indicates the hilus edge behind the postsynaptic processes) in a normal RS. In ***B***, postsynaptic processes are shown. In ***A*** the interior of the invagination reveals the diverticuli (asterisks), which reside between postsynaptic processes. In ***B*** note that the postsynaptic processes fill the hilus. ***C–E,*** Models of the hilus (black outline; dashed line in ***E*** indicates the hilus edge behind the postsynaptic processes) in two 7 d detached retinas. In ***C*** and ***D*** the hilus is greatly enlarged and could not be imaged completely in a single 400-nm-thick section. In ***C***, diverticuli, often absent in detached RS, are present (white asterisk). In ***D***, two HCATs (red and blue) are visible and do not fill the entire hilus. A relatively normal hilus (***E***) from a 7 d detached RS but only two postsynaptic HCs (red and blue) enter the hilus with significant extracellular space normally occupied by RB dendrites. Scale bars: 100 nm.

associated synaptic ribbons (albeit modified) bifurcating these indentations despite the lack of a true invagination (Fig. 4D).

In 7 d detached retinas, the size of the hilus was greatly enlarged, 497 ± 85 nm ($N = 8$, $\pm$SEM; Fig. 3D), compared with 314 ± 13 nm ($N = 17$, $\pm$SEM; Fig. 3D) the control (compare Fig. 5A,B with Fig. 5C,D). The expansion and distortion of the hilus shown in Figure 5, C and D, occurred to the extent that it was difficult to define, allowing the remaining internal infoldings of the invagination to be visible. In less extreme cases, the hilus appeared relatively normal, although there were only two postsynaptic processes extending through it, both identified as HCATs (Fig. 5E).

In general, important features of the normal RS, that is, tightly packed postsynaptic processes, the presence of RB dendrites and highly branched HCAT, a narrow hilus, and a singular synaptic ribbon had disappeared at 7 d of retinal detachment. In the RS of detached retinas, there was significantly more extracellular space surrounding the remaining postsynaptic processes (see Fig. 9C,F, asterisks). It was common to find only two processes, with general features of HCATs, and rather than branching to form the deep endings of telodendria, as in the normal RS, the HCATs had ended bluntly within the invagination (Figs. 2D', 3B'). Expansion of the hilus, an increase in the circularity and solidity of the invagination, indicating the loss of its complex branched structure, are all general characteristics of the RS in detached retina (Figs. 3D, 4F).

Organization of postsynaptic processes in the normal retina
Models derived by segmentation of the tomograms also illustrate the organization of postsynaptic processes within the invagination. Examples are shown in Figure 6, which shows the detailed

organization of the postsynaptic processes; Figure 6, A and C, show selected z-slices from two tomograms, illustrating the appearance of the postsynaptic complex in single sections. In Figure 6A, there appear to be two ribbons (R) with three postsynaptic processes opposite each, one rod bipolar dendrite (RB1, RB2), and two horizontal cell processes (H1, H2). Diverticuli from the RS (asterisk) lie between them. In this plane, the top H1 process can be seen to have a few synaptic vesicles, and the RS membrane opposite the RB dendrites is lined with densification (small arrows), defining characteristics for each. RB processes are typically devoid of vesicles. Figure 6C shows another example, in this case only one ribbon (R) is evident, and the hilus of the RS is visible between the black arrowheads. Figure 6, B and B' show two views of the 3-D model constructed from the tomogram in Figure 6A. In Figure 6B the model is clipped to show data from selected z-slices that reflect the structures shown in Figure 6A. In this case the synapse appears to have two triadic arrangements of postsynaptic processes opposite two ribbons. Figure 6B' shows the full model showing that there is in fact one long arching ribbon behind two horizontal cell processes and two rod bipolar dendrites. In Figure 6C' the model shows a similar arrangement of the postsynaptic processes. Within each model, diverticuli (asterisks) fill in space between the postsynaptic processes.

The configuration of the postsynaptic processes of the RS is often described as a triad in nonprimate mammals. Figure 6 demonstrates the importance of comprehensive 3-D reconstruction to understand their organization. Figure 6A shows a 2-D view, which appears to illustrate two such triads, each composed of two HCAT endings (H1, H2) and a single RB dendrite opposite a synaptic ribbon. Figure 6B reinforces this interpretation by partial reconstruction of the synapse. However, Figure 6B' shows the complete reconstruction of these processes as they terminate beneath the synaptic ribbon. The two ribbons in Figure 6, A and B, are in fact endings of the same arch-shaped ribbon, and the HCAT and RB endings form a complex of four postsynaptic processes (two from each cell type) associated with it. This same configuration can be seen in a single z-slice selected from another tomogram (Fig. 6C,C') where the two HCAT and RB dendrites terminate beneath the ribbon. Of nine complete tomograms, seven had a clear tetrad, one also contained an unidentified postsynaptic process (see Fig. 8), and one seemed likely to be a tetrad but lacked sufficient membrane resolution to be unambiguous. Therefore, images of complete reconstructions support a tetradic arrangement of the postsynaptic processes rather than a triadic one.

Additional models of the postsynaptic processes are shown in Figure 7. The architecture of the two types of processes were found to vary greatly once inside the invagination. RB processes appeared relatively narrow as they enter the invagination and terminated one- to two-thirds of the way within the invagination relative to the HCAT (Fig. 7B). They expanded slightly to form a slab-like blunt ending; they were never observed to branch. HC processes on the other hand expanded greatly within the invagination and curved to fill space just below the ribbon. They also branched to form readily identifiable small telodendria that terminate deep within the RS cytoplasm (Figs. 3A, 4A,B, 7A,C, white asterisks). As mentioned earlier, this prominent branching is readily identifiable by segmenting just the plasma membrane of the RS (Figs. 4A,B, 7B,C). The main body of the HCAT terminates directly adjacent to the synaptic ridge beneath the synaptic ribbon (Figs. 6, 7A, 8), whereas the small lollipop endings terminate deep in the RS cytoplasm. The organization of the HCATs can be complex within the invagination as they parallel the synaptic ribbon (Fig. 7C). The 3-D models show the extent of the
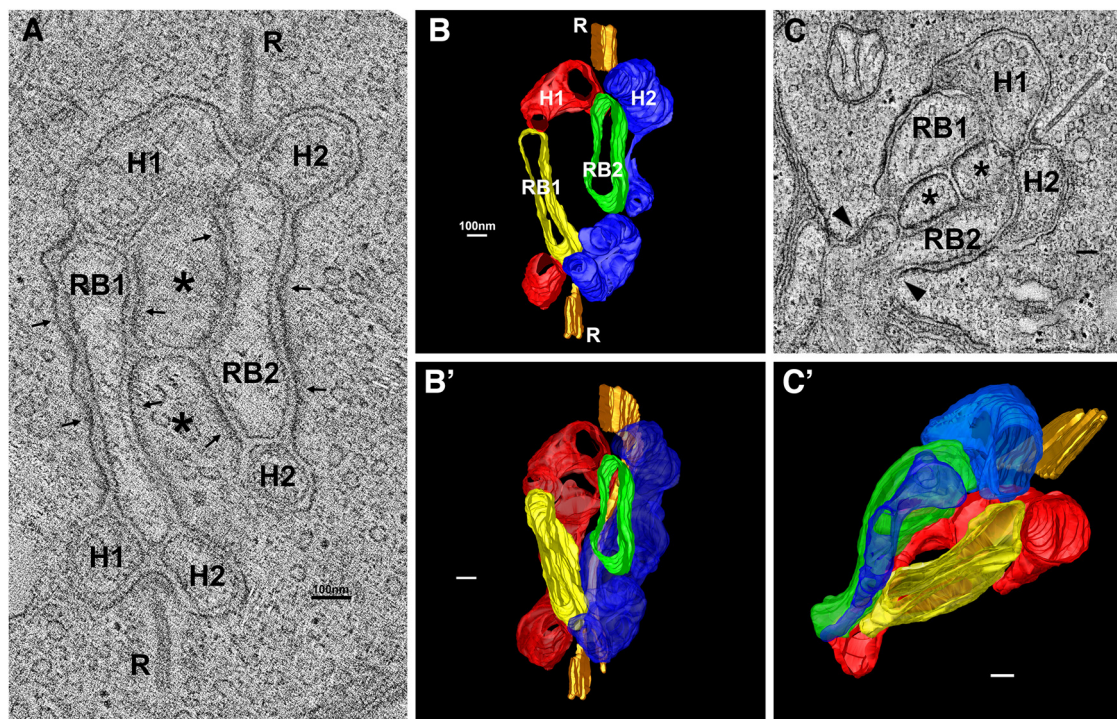
Figure 6. The organization of postsynaptic processes reveals a tetrad as the fundamental organizing unit. **A**, A z-slice of a tomogram selected to show an arrangement of two HC processes (H1, H2) and two rod bipolar processes (RB1, RB2) opposite apparent synaptic ribbons (R). The image also shows two of the diverticuli of RS cytoplasm (asterisks), which reside between postsynaptic processes, one of which (bottom) is still contiguous with the RS cytoplasm, and the other (top) appears independent in this plane. Densification of the RS plasma membrane occurs opposite the RB dendrites (small arrows). **B**, **B′**, Segmentation of the tomogram in **A**. In **B** several z-slices have been omitted to show two characteristic triads around two apparent synaptic ribbons as shown in **A**. **B′**, however, shows segmentation of the full volume indicating a simple arrangement of four postsynaptic processes opposite one synaptic ribbon. **C**, **C′**, A second example from another tomogram of the four postsynaptic processes opposite one ribbon. In **C** the asterisks indicate the diverticuli between the postsynaptic processes. The hilus is indicated by black arrowheads. Scale bars: 100 nm.

small lollipop endings. HCATs can form up to four to five of these terminal endings from the main HCAT volume. Overall, although RB dendrites are simple in their organization, HCATs are more complex in organization and structure than previously appreciated; some HCATs extend up to six independent lollipop endings, of which the functional implications are not clear.

Our tomography data from the normal cat has revealed an unexpected variation within some RSs. Figure 8A shows a single z-slice through the postsynaptic process of a RS, with the typical two HCAT (H) and two RB dendrites. But there is also an additional process (Fig. 8A, asterisk). In most z-slices, this process had the characteristics of a diverticulus. However, here, and in one other RS, it did not connect to the RS cytoplasm but rather entered the invagination through the hilus, where it terminated bluntly beneath the ribbon. When reconstructed, this process (Fig. 8B, white area) stands out as distinct from the HCAT and RB processes. In addition to the presence of vesicles (Fig. 8B, cyan spheres), these processes have membrane densification opposite the RB dendrites (Fig. 8A, black arrows), thus making it distinct from any other postsynaptic processes. Hence, we have identified an additional postsynaptic process in two RSs that arise from an unknown cell type.

Organization of postsynaptic processes in the 7 d detached retina

Beyond the general changes in RS organization mentioned here (see below, Results), the most striking other change in the RSs of detached retinas was the complete lack of identifiable RB dendrites within the invagination (Fig. 3C). In contrast, HCATs were still present; their identification was usually straightforward

because they contained cytoplasmic synaptic vesicles (even in detached retinas). However, they were extensively modified as they completely lack the complex branching characteristic of HCATs in normal retinas. Hence, the loss of RB dendrites and the complex branching of the HCATs creates excess extracellular space in the invagination in the RSs of 7 d detached retinas. Synaptic ribbons, albeit highly modified (see below), were still present and often lay in an identifiable bifurcation ridge that would typically separate the two HCATs (Fig. 9A,A′,C,C′,F,F′), even in RSs that did not have a clear invagination (Fig. 9D,D′).

The synaptic ribbon and vesicle populations in the normal retina

In single sections, the synaptic ribbon can appear as a typical straight-line structure (Fig. 10A); however, when adequately reconstructed, they formed a long arc that folded over a synaptic ridge opposite the postsynaptic complex (Figs. 10B, 11A). However, there was variation in the size and shape of the ribbon; we found ribbon lengths ranging from 214 to 1700 nm in the normal RS. We found convincing evidence for only a single ribbon per RS in all of our tomograms from normal feline retina.

The arciform density is a structural feature lying directly beneath the ribbon, within the synaptic ridge adjacent to the HC processes (Fig. 10B,E). It has been described as a V-shaped trough in which the ribbon sits (Zampighi et al., 2011). In our reconstructions, the arciform density was a continuous structure extending the full length of the ribbon (Fig. 10B,E). Like the ribbon, it is not a membrane-bound organelle. Zampighi et al. (2011) described pentamer structures that extend from the edges of the arciform density toward the ribbon. Here, we observed
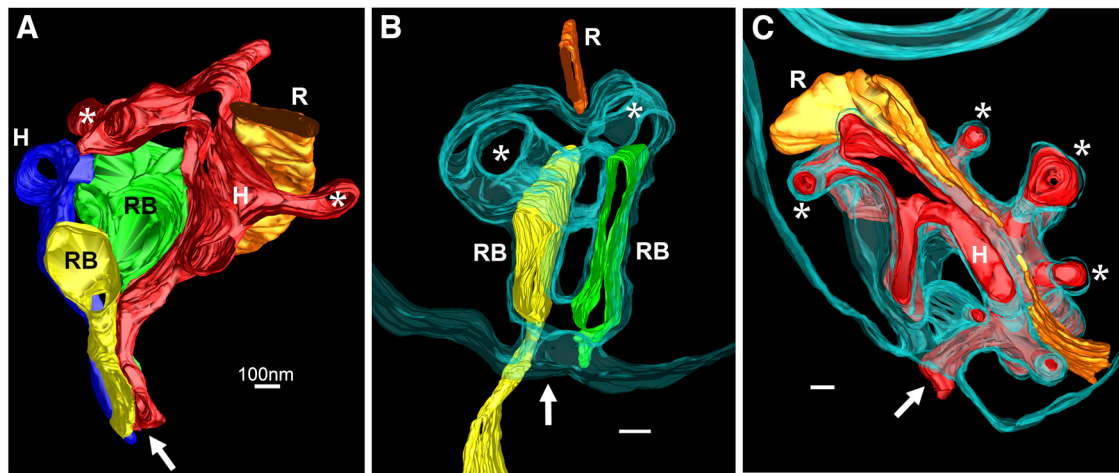
Figure 7. Structural organization of the different postsynaptic processes in normal retina. ***A***, The postsynaptic processes and synaptic ribbon from a healthy RS invagination. Note the complexity of the red HCAT as it branches around the ribbon giving rise to two of the lollipop-shaped endings (asterisk) on either side of the ribbon (R). Both RB cell dendrites end bluntly more distant from the ribbon. Only a portion of the blue HCAT was within the volume. ***B***, The synaptic invagination of a healthy RS, with only the RBs, the ribbon, and the RS membrane visible. The cyan plasma membrane of the RS is made transparent to show how the RB dendrites expand within the invagination to unbranched slab-like endings that terminate distant from the ribbon. Asterisks mark the location of HCAT adjacent to the ribbon (R). The arrows mark the hilus. ***C***, An RS invagination with just the ribbon, a singular HCAT, and a translucent RS membrane visible. In this image, the model is oriented to show the complex branching of the HCAT (red) adjacent to the synaptic ribbon (orange). Asterisks indicate the lollipop endings of the HCATs. The HCAT enters the invagination at the hilus (arrow). Scale bars: 100 nm.

similar electron-dense structures ~25 nm in size extending along the full length of the arciform density with a spacing of 35–45 nm (Fig. 10*E*, white arrows). Fundamentally, the arciform density appeared as a continuous structure that lined the entire extent of the ribbon. This observation contrasts with the previous reports of two separate arciform densities at each synapse (Migdale et al., 2003; Tsukamoto and Omi, 2022).

In normal RSs, there are three different states that synaptic vesicles of typical size (~25 nm) can occur in—free throughout the cytoplasm, associated with the synaptic ribbon (Fig. 10*A*–*C*, magenta spheres). and fused to the RS membrane. Although data from single ultrathin sections have suggested that the vesicle population across RS is quite similar, our tomographic reconstructions, capable of showing three to four times the volume of an ultrathin section, suggested that there may be variability from one RS to the next, as shown in comparison of the left RS and the two right RSs in Figure 2*C*'. Ribbon-associated vesicles generally pattern the synaptic ribbon along its length. In single sections these can appear to be uniformly and evenly spaced (Fig. 10*A*,*C*) and have generally been depicted in this configuration. However, our tomographic reconstructions show that they are not necessarily evenly distributed over the surface of the ribbon (Figs. 10*B*, 11*A*). Many vesicles can be seen clearly fused with the RS membrane (Fig. 10*D*, green arrows), engaging in active synaptic transmission. Interestingly, although vesicular fusion events do occur near the synaptic ribbon, the assumed site of synaptic transmission, a large number of fused vesicles were also observed far away from this region, primarily adjacent to the small HCAT telodendria (Fig. 10*F*, red spheres). Zampighi et al. (2011) also described vesicle fusion in regions other than at the synaptic
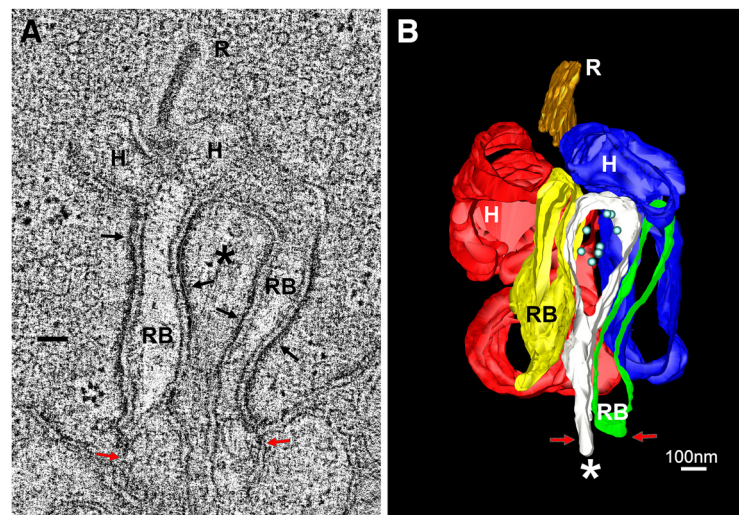

Figure 8. An additional unidentified process occurs at some synapses. ***A***, ***B***, A representative *z*-slice from a tomogram of a normal RS showing an unidentified process (asterisk) terminating within the invagination (***A***). A segmentation of this tomogram (***B***) where two HCATs (H, red and blue) and two RB dendrites (yellow and green) were identified in addition to the unusual process (white asterisk). This process has ultrastructural characteristics of RS cytoplasm (membrane densification opposite the RB processes, black arrows in ***A***), and the presence of several intracellular vesicles (cyan spheres in ***B***). However, the process originates within the OPL and enters the invagination through the hilus (red arrows). Scale bars: 100 nm.

ribbon and suggested they may be involved in transmitter release or alternatively as sites of vesicular membrane recovery.

An identifying feature of HCATs is the presence of intracellular vesicles. Although similar to traditional synaptic vesicles, they are typically larger in diameter (~45 vs ~25 nm) and with more variation in size and shape (Fig. 11*A*,*B*). They were generally scattered throughout the HCAT but were aggregated in the lollipop endings (Fig. 11*A*, cyan arrow). We also found dense core vesicles (DCVs) in the HCAT processes (Fig. 10*D*, black arrow; Fig. 11*B*, large spheres in the red HCAT). DCVs have been reported to occur near neuronal synapses where they most likely participate in some form of a paracrine type of response affecting neurons differently
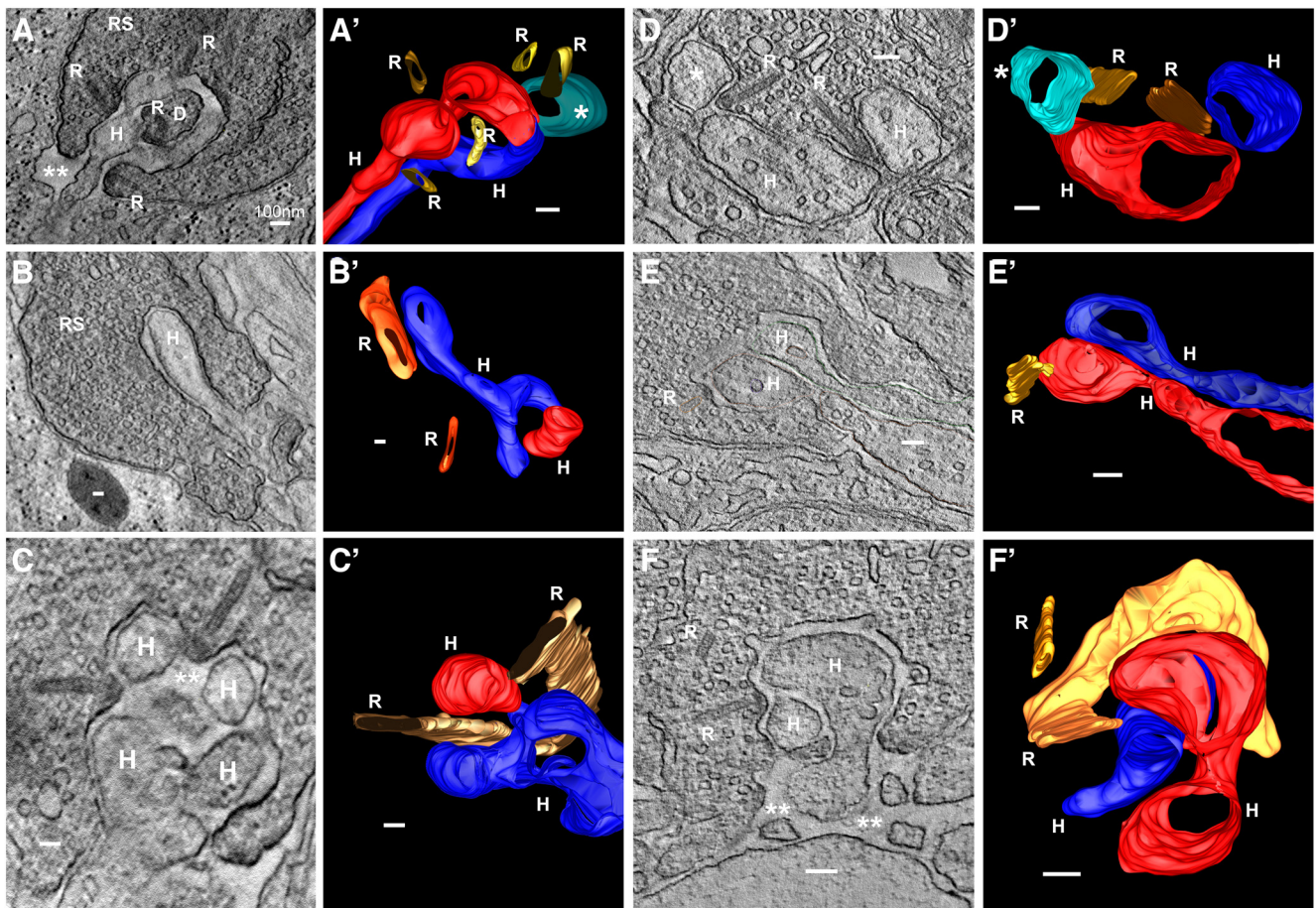
Figure 9. Rod spherules after a 7 d detachment. They have a greatly simplified organization and show the loss of RB dendrites; HCATs have lost their complex branching, including the small lollipop endings, there are often multiple synaptic ribbons, and there is increased extracellular space within the invagination. *A–F'*, Representative *z*-slices of tomograms (left, *A–F*) and their 3-D models (right, *A'–F'*). Simplistic HCATs lacking telodendria, with multiple synaptic ribbons (*A*, *B*, *E*). An additional unidentified process is evident in *A*. All postsynaptic processes that were positively identified arose from HCATs. *A'* and *D'* each contain a process that could not be positively identified as an HCAT because of a lack of intracellular vesicles but were not able to be positively identified as RB dendrites either because of a lack of membrane densification (these processes are shown in cyan, labeled with a white asterisk). *C* and *F* depict extremely arced and distorted synaptic ribbons, a shrunken synaptic invagination, and a large amount of extracellular space (white double asterisks). *D* contains an RS that lacks an invagination entirely and only has slightly indenting postsynaptic processes that lie between multiple bifurcating synaptic ribbons. Extracellular space not found in normal RS is indicated by white double asterisks in *A*, *C*, and *F*, and a diverticulum (white D) is shown in *A*. Scale bars: 100 nm.

than the vesicles participating in typical neuronal signaling (Kuznetsov and Kuznetsov, 2017; Trueta, 2021). However, their exact role at the rod synapse is not clear.

The synaptic ribbon and vesicle populations in the 7 d detached retina

All the reconstructed RSs in 7 d detached retinas still had identifiable synaptic ribbons, and in single sections the morphology of some ribbons in detached retinas appeared similar to those in normal retinas. However, when viewed in tomographic volumes, it was clear that the organization of most ribbons was greatly altered by detachment. Most striking was their increase in number, decrease in size, and their altered location within the spherule cytoplasm (Figs. 4, 9, 10G,H). Many assumed a very different shape in comparison with those in normal retinas. For example, the two apparent ribbons in the *z*-slice shown in Figure 9C are the result of sectioning through the ends of a highly curved ribbon that is almost U shaped (Fig. 9C'). In a normal RS, the ribbon is not as highly curved. The larger ribbons shown in Figure 9, *C'* and *F'*, contain a clear twist. In a normal cat RS, there is always just one ribbon. In a 7 d detached retina, the number of

independent ribbons can vary from one (Fig. 9C',E'), to two (Figs. 9B',D',F', 10G) or more (Figs. 3B, 4C, 9A, 10H). A major difference in the detached retina was the appearance of short ribbons, often lying close to, but not connected to, a larger more traditional ribbon, suggesting they had fragmented from the larger ribbon (Fig. 10G,H). The average ribbon length after retinal detachment decreased from $0.7 \pm 0.09\,\mu m$ ($N = 22$, $\pm$SEM) in the normal retina to $0.3 \pm 0.07\,\mu m$ ($N = 18$, $\pm$SEM) in the detached retina (Fig. 3D; $p = 0.0003$), and the ribbon quantity per spherule doubled (Fig. 3C; $p = 0.00,008$). Sometimes, these smaller ribbons had no vesicles associated with them (Fig. 4C, top ribbon). In detached retinas, ribbons that maintained their proximity to postsynaptic processes (i.e., adjacent to the RS membrane) had an identifiable arciform density (Figs. 3B, 9C,E,F), whereas those that lay free in the cytoplasm did not.

In the normal RS, vesicles lay adjacent to the entire ribbon at a defined distance and relatively uniform distribution (Fig. 10A–C). In detachment, this association appeared looser, with vesicles sometimes forming a sparsely populated cloud around the ribbons (Fig. 10G,H). Although segmentation of these vesicles in a normal RS is relatively straightforward, it was difficult to assign
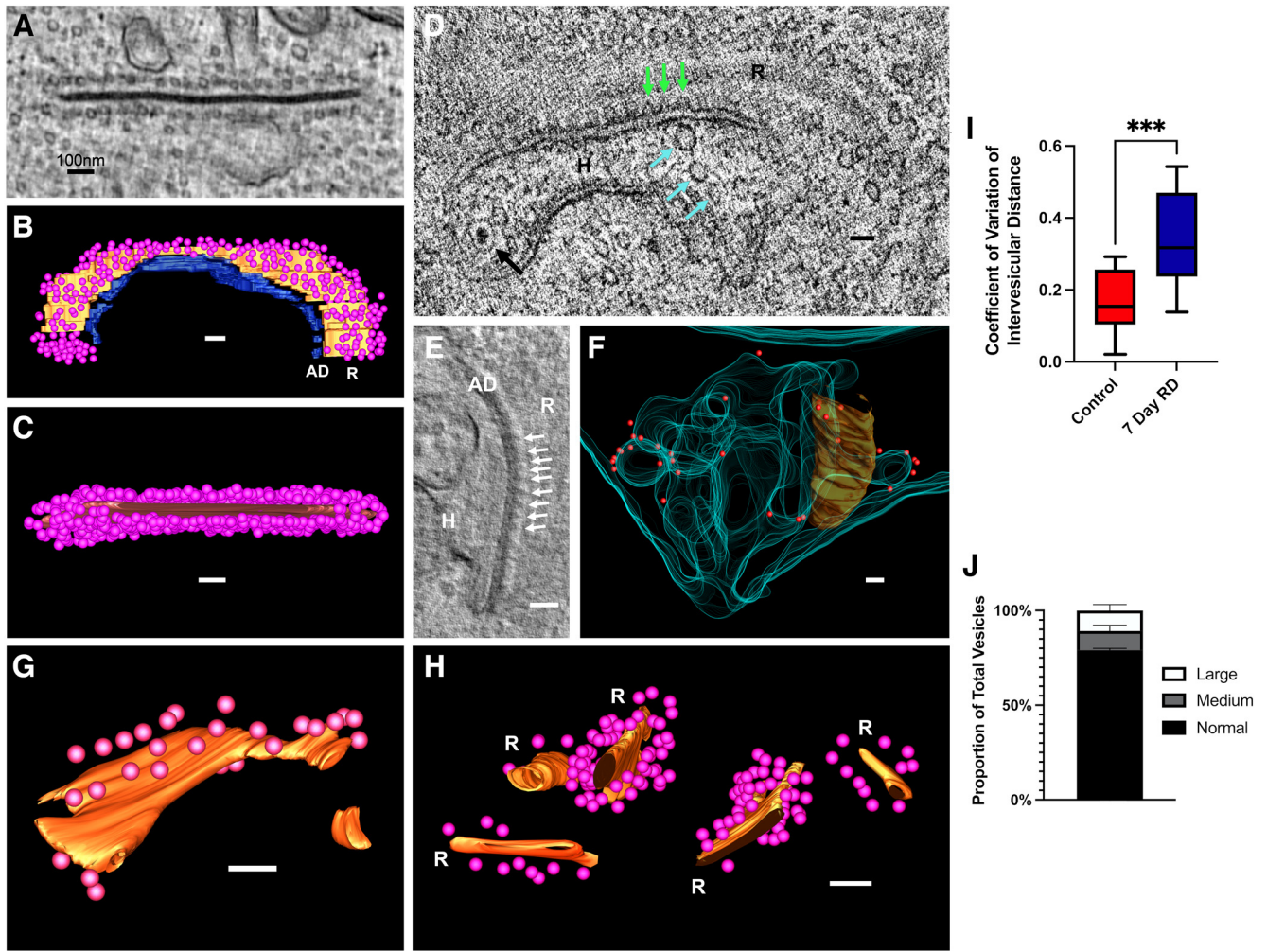
Figure 10. Synaptic ribbons and vesicles in normal and 7 d detached retina. ***A***, A representative *z*-slice from a tomogram of a normal synaptic ribbon with characteristic patterning of synaptic vesicles along its length. ***B***, A model derived from the segmentation of a synaptic ribbon (orange) with its associated vesicles and arciform density (blue); the arciform density is a thin layer that underlies the length of the ribbon. Note that vesicles are scattered over the surface of the ribbon. ***C***, The same model as in ***B*** but viewed from top-down angle where vesicles appear uniformly clustered on the ribbon. ***D***, A representative *z*-slice from a tomogram of a normal synaptic ribbon (R) arcing around an HCAT (H). Synaptic vesicles are fused to the RS membrane opposite the HCAT (green arrows). Also shown are intracellular HCAT vesicles (cyan arrows), as well as a characteristic dense core vesicle (black arrow). ***E***, A z-slice from a tomogram showing electron dense projections (white arrows) extending from the arciform density toward the synaptic ribbon (R) which is sectioned *en face*. ***F***, A normal synaptic invagination with its membrane (cyan) made semitransparent. The synaptic ribbon is in orange (dimly lit, behind the RS membrane), and nonribbon associated vesicles fused to the RS membrane are red spheres. ***G***, ***H***, Models of synaptic ribbons from 7 d detached retina, showing ribbon fragments with sparse and often unorganized associated vesicles. ***I***, Analysis of the spacing of synaptic vesicles along the ribbon. The distance between ribbon-associated vesicles was measured, and the coefficient of variation (SD/mean) was plotted as a measure of variability on a box and whisker plot. Each data point represents the intervesicular spacing variability along a single ribbon. Student's *t* tests were used to determine the probability of no significant difference (see above, Materials and Methods for further statistical details). ***J***, The proportion of different types of cytoplasmic vesicles present in the 7 d detached rod spherules; **$p < 0.005$, ***$p < 0.0005$, ****$p < 0.00005$. Scale bars: 100 nm.

vesicle locations relative to the ribbon in the detached retina. This is further described by the large increase in the coefficient of variation (SD/mean) of the distance between ribbon-associated vesicles (Fig. 10*I*). The 7 d detached RS had more than twice the spacing variability compared with the control.

Although vesicles associated with synaptic transmission were still observable in the detached retina—free in the RS cytoplasm, associated with the synaptic ribbon, and in the HC processes—major differences appeared in vesicle fusion, the appearance of large swollen cytoplasmic vesicles, and their distribution within the HC processes. Despite being easily found in the control, we were unable to identify a single vesicle fused to the RS plasma membrane in the detached condition. Within degenerating RSs we also found the presence of two new vesicle morphologies, those slightly larger than synaptic vesicles (~45 nm; Fig. 11*C*, blue arrows) and much larger swollen vesicles (Fig. 11*C*, red

arrows; Fig. 10*J*). The intracellular HCAT vesicles also have some slight changes; they were usually fewer in number and more scattered throughout the process (Fig. 11*D*) where it enters the invagination.

Hence, 7 d of retinal detachment results in a greater number of synaptic ribbons, a reduction in consistency of synaptic vesicle association with the synaptic ribbons, and a complete lack of vesicle fusion along the membrane, indicating that synaptic transmission after detachment is likely significantly impaired.

Discussion
By exploiting the high *z*-resolution of EM tomography, we have added significantly to our knowledge of the RS, the first synapse of scotopic vision and one of the most complex synapses in the CNS. In particular, we have shown the extent and complexity of
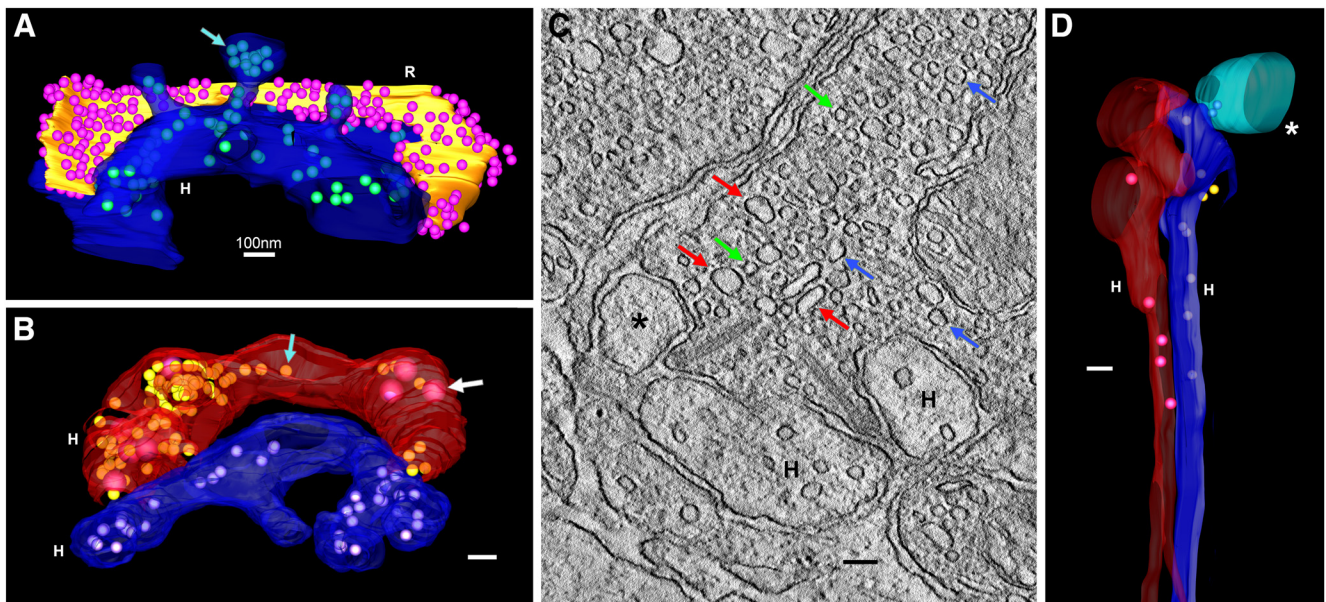
Figure 11. Retinal detachment leads to changes in cytoplasmic and intracellular vesicles. **A**, An HC process (blue) in normal retina opposite its synaptic ribbon (orange). The HCATs often have large numbers of intracellular vesicles, with special accumulation in the lollipop endings (cyan arrow). **B**, Another pair of HCATs in normal retina depicting both a large population of typical synaptic vesicles (cyan arrow) as well as a number of larger dense-core vesicles (white arrow). **C**, A z-slice from a tomogram of 7 d detached RS containing a range of intracellular vesicles. There is a large number of typical synaptic vesicles (green arrows), a few vesicles of larger size (blue arrows), and a few swollen vesicles that are of variable shape and size (red arrows). **D**, A model showing two HCATs (H, red and blue) in a 7 d detached retina with a reduced population of intracellular vesicles. The process marked with the asterisk was unidentified. Scale Bars: 100 nm.

the synaptic invagination and have provided new evidence for interpreting the organization of the postsynaptic processes. Our results have shown that tomography is valuable in resolving contradictory descriptions for the organization of this synapse. Additionally, we have provided the first high-resolution description of changes these synapses undergo during retinal injury in the context of a 7 d retinal detachment, where the organization of the RS breaks down significantly.

Organization of the postsynaptic processes
The organization and especially the number and types of cells contributing to postsynaptic processes in the RS is fundamental to retinal circuitry. Yet, there has been confusion over these processes since their earliest descriptions by Sjöstrand (1958) and Missotten (1965). A triadic organization has been commonly reported, consisting of two lateral HC processes and a centrally located RB dendrite (Mariani, 1984; Maslim and Stone, 1986). However, Rao-Mirotznik et al. (1995) described the processes as a tetrad in cat, and Migdale et al. (2003) described them as organized into two synaptic units in cat, monkey, and human, with each unit having two lateral elements and one or more central elements. Tsukamoto and Omi (2022) described 10 different types of pattern in Macaque RS and one type (a tetrad) in mouse. The limited z-axis resolution in reconstructions from conventional EM serial sections has contributed to these different interpretations. As shown in Figure 6, the arc shape of the synaptic ribbon can easily lead to the conclusion that the processes occur in two triadic arrangements. However, our tomographic reconstructions suggest that the tetrad is the most accurate description in cat. It is likely that high-resolution reconstruction of this synapse in other species will also show the tetrad to be the most common fundamental organizational unit in mouse and other non-primate mammals. Signaling from a rod spherule to two RB cells (as in a tetrad) rather than just one (as in a triad) might be a way of countering intrinsic noise in the RB cells.

The number of synaptic ribbons remains controversial, in large part because of their very large size and arcuate shape. On full reconstruction of large 3-D volumes, we identified only one ribbon in each RS. This conclusion is in agreement with Migdale et al.'s (2003) conclusion for cat retina; however, they concluded there were two arciform densities associated with each ribbon, defining two synaptic units for each RS. Tsukamoto and Omi (2022) identified one or two ribbons and two arciform densities in each mouse RS. In our high-resolution reconstructions we found no evidence for a break in the continuity of the arciform density, suggesting there is only one long site of transmitter release associated with each synaptic ribbon. Thus, our results are most compatible with a simple grouping of four postsynaptic processes opposite a single ribbon and single arciform density. Moreover, our imaging of the normal hilus (Fig. 5) shows that four synaptic processes (two HCs and two RBs) enter the invagination, indicating that terminal branching does not underlie the appearance of four processes within the invagination.

We also found 2 of 14 normal synapses that had a third type of postsynaptic process (Fig. 8). A process with this shape and location within the invagination was identified as a HCAT in Kolb (1970) and as an RB dendrite (https://webvision.med.utah.edu/book/part-iii-retinal-circuits/circuitry-for-rod-cells-through-the-retina/). Its ultrastructural characteristics most closely match those of the diverticuli that enter the invagination as internal branches of the spherule itself (i.e., the presence of both synaptic vesicles and membrane densification), but in both cases it enters the invagination through the hilus from the outer plexiform layer. To our knowledge, there is no known candidate cell type reported in the literature of mammalian retinas that could account for this process.

Major ultrastructural degeneration in 7 d detachment
As suggested previously (Linberg et al., 2009), 7 d of retinal detachment resulted in most RSs showing ultrastructural signs of severe degeneration. Here, we show that this includes a
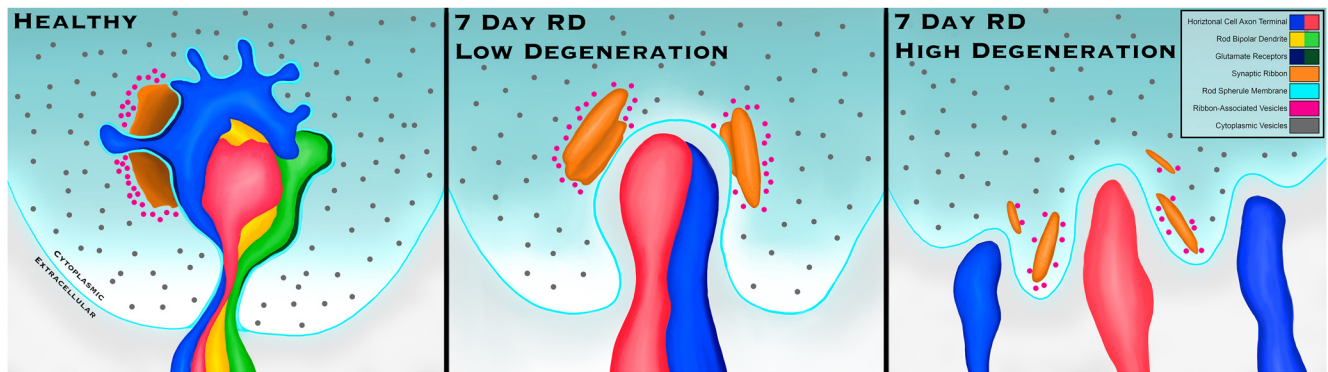
Figure 12. Schematic figure describing the key ultrastructural changes occurring in the rod spherule during a retinal detachment. There is variation in the extent of degeneration from one spherule to the next, and so we have depicted two different levels of degeneration within RS. Left, In the healthy RS, there are four (occasionally 5) postsynaptic processes made up of two horizontal cell axon terminals and two rod bipolar cell dendrites. A synaptic ribbon surrounds the HCATs along the edge of the invagination as the spherule membrane tightly contours these postsynaptic processes. Middle, In lower levels of degeneration, the complex contours of the invaginating membrane are lost, leaving a heavily simplified structure. Bipolar cell processes generally retract, leaving only HCATs that are left surrounded by large amounts of extracellular space. The hilus greatly expands, and the synaptic ribbons fragment resulting in two or more synaptic ribbons with sparse and variable vesicle associations. Right, In the most highly degenerated synapses, the postsynaptic cells no longer enter the hilus and simply lie as indents along the spherule membrane. The ribbon often fragments and in some cases is present with no associated vesicles. The entire synaptic structure falls apart, likely leading to a complete inability to send synaptic signals.

remodeling of the complex contour of the invagination itself, in some cases proceeding to only minor indentations of the RS base. In the degenerating RS, the greatly simplified HCATs remained associated with the terminal, even when the invagination was almost entirely lost (Figs. 9, 11). RB dendrites, however, were lost from every postdetachment RS we examined, consistent with results from previous studies. (Linberg et al., 2006a, 2009; Townes-Anderson et al., 2021). The synaptic ribbon appeared to become fragmented into small ribbons, which often appeared free in the RS cytoplasm, seemingly no longer anchored to a synaptic site, an observation never seen in normal retinas. The approximate doubling in the number of ribbons, together with the halving of ribbon length, implies that overall ribbon length per spherule was nevertheless conserved. Ultrastructurally, the small ribbons appeared best described as fragments of the original ribbon (Figs. 9, 10G,H), but we cannot rule out the possibility that they were synthesized *de novo* (Fig. 12).

We also identified, in normal retinas, 25 nm projections that extended toward the synaptic ribbon from the arciform density. Bassoon, a large 420 kDa protein, vitally important for anchoring the ribbon to the invagination (Dick et al., 2003), is a likely candidate for forming these projections (Brandstätter et al., 1999). The arciform density was difficult to study in degenerated synapses because of its small size and the disorganization of the synapse, but our limited observations suggest that these features were indeed maintained but only associated with ribbons that remained closely apposed to the presynaptic membrane (Figs. 3B, 9C,E,F). Ribbon fragments that were not in close apposition to the membrane appeared to float in the cytoplasm without an arciform density.

Remodeling of the hilus in the detached retina was profound and would likely have important functional ramifications. The normal hilus was filled with the processes from postsynaptic neurons (Fig. 5A,B). In most degenerating RSs the hilus became greatly enlarged (Figs. 5C,D; Linberg et al., 2009), and, even when its size was maintained, it was no longer filled with neurites because of the retraction of RB dendrites (Fig. 5E). The remodeling of postsynaptic processes also greatly increased the extracellular space within the invagination. Thus, the normally compact, isolated internal environment of the synaptic invagination was lost and became continuous with the extracellular space of the outer plexiform layer. Presumably, any glutamate released from the photoreceptors would no longer be confined to the synaptic invagination; it would be free to diffuse into the retina and may account for the spike in retinal glutamate suggested to occur during the first 3 d after a retinal detachment in cat (Marc et al., 1998). Glutamate is a potent excitotoxin that can cause rod photoreceptor cell death (Charles-Messance et al., 2020) and changes in the inner retina (Bringmann et al., 2013), including gliosis of Müller cells (Ji et al., 2012) and degenerative changes in neurons (Yang, 2004; Yee et al., 2018; Milla-Navarro et al., 2021). Detachment produces rapid photoreceptor cell death (Cook et al., 1995), gliotic responses in Müller cells (Lewis et al., 2010), as well as aberrant sprouting of neurites from RB, horizontal, and ganglion cells (Lewis et al., 1998; Coblentz et al., 2003; Linberg et al., 2006b) possibly induced by excess glutamate in the retinal environment.

In normal retinas, synaptic vesicles fused to the RS plasma membrane at both the active zone and far from it, usually opposite the lollipop-shaped endings of the HCAT (Fig. 10). Evidence suggests that vesicle release at these two locations use different synaptotagmins and that the nonribbon release plays a more modulatory role (Mesnard et al., 2021) that is currently not well understood. In detached retinas, we found no evidence for vesicle fusion at either site in detached retina, a further indication that detachment interrupts the flow of information into the rod pathway. We did, however, observe that ribbon-associated vesicles remained, even in association with very small ribbons (Fig. 10H). The population of free vesicles was highly heterogenous with the inclusion of many large vesicles (Fig. 11). There is evidence for vesicle-to-vesicle fusion that may occur before their fusion to the RS membrane as a mechanism for multiquantal release (Mesnard et al., 2021). In the degenerated state, there may be an imbalance in vesicle production and release resulting in a significant increase in the heterogeneity of the vesicle population.

The presence of a dense population of synaptic vesicles in the HCAT lollipop-shaped endings is congruent with physiological evidence for synaptic feedback from horizontal cells to rod photoreceptors (Thoreson et al., 2008). Only two studies, one in human and one in macaque, have found ultrastructural evidence for identifiable presynaptic sites in the HCAT (Linberg and

Fisher, 1988; Tsukamoto and Omi, 2022). These sites are atypically small, but it seems unlikely we would have overlooked them in the tomograms, suggesting that the synaptic feedback in many species is nontraditional in form. Interestingly, we found that HCATs continued to express these vesicles even in a highly degenerated state and after the loss of their lollipop-shaped endings.

The changes we have identified in RS in detached retina likely have profound effects ranging from loss of the primary pathway for sending signals to the inner retina, to a disturbance in glutamate homeostasis. Based on our results and those from previous studies (Linberg et al., 2006b, 2009), within the 7 d detachment time period, the RB dendrites withdraw, leaving behind significant extracellular space (Figs. 2D, 3B) within the synaptic invagination and an open hilus, and the HCATs remodel, losing their small lollipop-shaped terminals and ending bluntly within the invagination. Thus, recovery of this synapse would seem to have several challenges, including virtually the complete rebuilding of the rod–RBC pathway. Indeed, there is now evidence that photoreceptor synapses may have very limited capacity for recovery (Townes-Anderson et al., 2021), stressing the need for early intervention or therapeutics that will enhance recovery.

Perspective

Our EM tomography results indicate that the basic organizational structure of the rod synapse is a tetrad arrangement of postsynaptic processes. During 7 d of retinal detachment, significant simplification of the rod synapse occurs, a change that is likely relevant to other photoreceptor degenerative conditions as well. Importantly, in retinal detachment patients, it is common to have reasonable anatomic recovery of the outer segment layer (Guérin et al., 1989, 1993) while significant visual deficits often remain; it is likely that degeneration of rod synapses plays a significant role in this outcome. Moving forward, it will be important to study the timescale of these restructuring changes relative to outer segment degeneration, understand the mechanisms of the degenerative changes, and gain an understanding of the ability of the synapse to recover.

References

Brandstätter JH, Fletcher EL, Garner CC, Gundelfinger ED, Wässle H (1999) Differential expression of the presynaptic cytomatrix protein bassoon among ribbon synapses in the mammalian retina. Eur J Neurosci 11:3683–3693.

Bringmann A, Grosche A, Pannicke T, Reichenbach A (2013) GABA and glutamate uptake and metabolism in retinal glial (Müller) cells. Front Endocrinol (Lausanne) 4:48.

Burette AC, Lesperance T, Crum J, Martone M, Volkmann N, Ellisman MH, Weinberg RJ (2012) Electron tomographic analysis of synaptic ultrastructure. J Comp Neurol 520:2697–2711.

Charles-Messance H, Blot G, Couturier A, Vignaud L, Touhami S, Beguier F, Siqueiros L, Forster V, Barmo N, Augustin S, Picaud S, Sahel J-A, Rendon A, Grosche A, Tadayoni R, Sennlaub F, Guillonneau X (2020) IL-1β induces rod degeneration through the disruption of retinal glutamate homeostasis. J Neuroinflammation 17:1.

Coblentz FE, Radeke MJ, Lewis GP, Fisher SK (2003) Evidence that ganglion cells react to retinal detachment. Exp Eye Res 76:333–342.

Collin GB, Shi L, Yu M, Akturk N, Charette JR, Hyde LF, Weatherly SM, Pera MF, Naggert JK, Peachey NS, Nishina PM, Krebs MP (2022) A splicing mutation in *Slc4a5* results in retinal detachment and retinal pigment epithelium dysfunction. Int J Mol Sci 23:2220.

Cook B, Lewis GP, Fisher SK, Adler R (1995) Apoptotic photoreceptor degeneration in experimental retinal detachment. Invest Ophthalmol Vis Sci 36:990–996.

Dick O, tom Dieck S, Altrock WD, Ammermüller J, Weiler R, Garner CC, Gundelfinger ED, Brandstätter JH (2003) The presynaptic active zone protein bassoon is essential for photoreceptor ribbon synapse formation in the retina. Neuron 37:775–786.

Erickson PA, Fisher SK, Anderson DH, Stern WH, Borgula GA (1983) Retinal detachment in the cat: the outer nuclear and outer plexiform layers. Invest Ophthalmol Vis Sci 24:927–942.

Grünert U, Martin PR (1991) Rod bipolar cells in the macaque monkey retina: immunoreactivity and connectivity. J Neurosci 11:2742–2758.

Guérin CJ, Anderson DH, Fariss RN, Fisher SK (1989) Retinal reattachment of the primate macula. Photoreceptor recovery after short-term detachment. Invest Ophthalmol Vis Sci 30:1708–1725.

Guérin CJ, Lewis GP, Fisher SK, Anderson DH (1993) Recovery of photoreceptor outer segment length and analysis of membrane assembly rates in regenerating primate photoreceptor outer segments. Invest Ophthalmol Vis Sci 34:175–183.

Ji M, Miao Y, Dong L-D, Chen J, Mo X-F, Jiang S-X, Sun X-H, Yang X-L, Wang Z (2012) Group I mGluR-mediated inhibition of Kir channels contributes to retinal Müller cell gliosis in a rat chronic ocular hypertension model. J Neurosci 32:12744–12755.

Kolb H (1970) Organization of the outer plexiform layer of the primate retina: electron microscopy of Golgi-impregnated cells. Philos Trans R Soc Lond B Biol Sci 258:261–283.

Kremer JR, Mastronarde DN, McIntosh JR (1996) Computer visualization of three-dimensional image data using IMOD. J Struct Biol 116:71–76.

Kung F, Wang W, Tran TS, Townes-Anderson E (2017) Sema3A reduces sprouting of adult rod photoreceptors *in vitro*. Invest Ophthalmol Vis Sci 58:4318–4331.

Kuznetsov IA, Kuznetsov AV (2017) How dense core vesicles are delivered to axon terminals—a review of modeling approaches. In: Modeling of microscale transport in biological processes. (Becker SM, ed), pp 335–352. Amsterdam: Academic.

Lewis GP, Linberg KA, Fisher SK (1998) Neurite outgrowth from bipolar and horizontal cells after experimental retinal detachment. Invest Ophthalmol Vis Sci 39:424–434.

Lewis GP, Chapin EA, Luna G, Linberg KA, Fisher SK (2010) The fate of Müller's glia following experimental retinal detachment: nuclear migration, cell division, and subretinal glial scar formation. Mol Vis 16:1361–1372.

Li S, Mitchell J, Briggs DJ, Young JK, Long SS, Fuerst PG (2016) Morphological diversity of the rod spherule: a study of serially reconstructed electron micrographs. PLoS One 11:e0150024.

Linberg KA, Fisher SK (1988) Ultrastructural evidence that horizontal cell axon terminals are presynaptic in the human retina. J Comp Neurol 268:281–297.

Linberg KA, Lewis GP, Matsumoto B, Betts KE, Fisher SK (2006a) Changes in the morphology and connectivity of rod spherules after experimental retinal detachment: an immunocytochemical and ultrastructural study. Invest Ophthalmol Vis Sci 47:4224–4224.

Linberg KA, Lewis GP, Matsumoto B, Fisher SK (2006b) Immunocytochemical evidence that rod-connected horizontal cell axon terminals remodel in response to experimental retinal detachment in the cat. Mol Vis 12:1674–1686.

Linberg KA, Lewis GP, Fisher SK (2009) Retraction and remodeling of rod spherules are early events following experimental retinal detachment: an ultrastructural study using serial sections. Mol Vis 15:10–25.

LoGiudice L, Matthews G (2009) The role of ribbons at sensory synapses. Neuroscientist 15:380–391.

Marc RE, Murry RF, Fisher SK, Linberg KA, Lewis GP (1998) Amino acid signatures in the detached cat retina. Invest Ophthalmol Vis Sci 39:1694–1702.

Mariani AP (1984) The neuronal organization of the outer plexiform layer of the primate retina. In: International review of cytology. (Bourne GH, Danielli JF, Jeon KW, eds), pp 285–320. Amsterdam: Academic.

Martin-Gutierrez MP, Buckley TM, MacLaren RE (2022) Chronic untreated retinal detachment in a patient with choroideremia provides insight into the disease process and potential therapy. Eur J Ophthalmol 32:NP30–NP33.

Maslim J, Stone J (1986) Synaptogenesis in the retina of the cat. Brain Res 373:35–48.

Matthews G, Sterling P (2008) Evidence that vesicles undergo compound fusion on the synaptic ribbon. J Neurosci 28:5403–5411.

Mesnard C, Hays C, Grassmeyer J, Barta CL, Hinz KK, Thoreson W (2021) Synaptotagmins 1 and 7 in vesicle release from rods and cones of mouse retina. Invest Ophthal Vis Sci 62:2003.

Migdale K, Herr S, Klug K, Ahmad K, Linberg K, Sterling P, Schein S (2003) Two ribbon synaptic units in rod photoreceptors of macaque, human, and cat. J Comp Neurol 455:100–112.

Milla-Navarro S, Diaz-Tahoces A, Ortuño-Lizarán I, Fernández E, Cuenca N, Germain F, de la Villa P (2021) Visual disfunction due to the selective effect of glutamate agonists on retinal cells. Int J Mol Sci 22:6245.

Missotten L (1965) The ultrastructure of the retina. Brussels: Editions Arscia.

Nash BM, Loi TH, Fernando M, Sabri A, Robinson J, Cheng A, Eamegdool SS, Farnsworth E, Bennetts B, Grigg JR, Chung S-K, Gonzalez-Cordero A, Jamieson RV (2021) Evaluation for retinal therapy for *RPE65* variation assessed in hiPSC retinal pigment epithelial cells. Stem Cells Int 2021:4536382.

Phan S, Boassa D, Nguyen P, Wan X, Lanman J, Lawrence A, Ellisman MH (2017) 3D reconstruction of biological structures: automated procedures for alignment and reconstruction of multiple tilt series in electron tomography. Adv Struct Chem Imaging 2:8.

Rao-Mirotznik R, Harkins AB, Buchsbaum G, Sterling P (1995) Mammalian rod terminal: architecture of a binary synapse. Neuron 14:561–569.

Rodieck RW (1998) The first steps in seeing. Sunderland, MA: Sinauer.

Sjöstrand FS (1958) Ultrastructure of retinal rod synapses of the guinea pig eye as revealed by three-dimensional reconstructions from serial sections. J Ultrastruct Res 2:122–170.

Sørensen NB, Christiansen AT, Kjaer TW, Klemp K, la Cour M, Heegaard S, Warfvinge K, Kiilgaard JF (2020) Loss of retinal tension and permanent decrease in retinal function: a new porcine model of rhegmatogenous retinal detachment. Acta Ophthalmol 98:145–152.

Sterling P, Cohen E, Freed MA, Smith RG (1987) Microcircuitry of the on-beta ganglion cell in daylight, twilight, and starlight. Neurosci Res Suppl 6:S269–285.

Thoreson WB, Babai N, Bartoletti TM (2008) Feedback from horizontal cells to rod photoreceptors in vertebrate retina. J Neurosci 28:5691–5695.

Townes-Anderson E, Halasz E, Wang W, Zarbin M (2021) Coming of age for the photoreceptor synapse. Invest Ophthalmol Vis Sci 62:24.

Trueta C (2021) An analytical method to measure the contribution of clear synaptic and dense-core peri-synaptic vesicles to neurotransmitter release from synaptic terminals with two classes of secretory vesicles. MethodsX 8:101374.

Tsukamoto Y, Omi N (2022) Multiple invagination patterns and synaptic efficacy in primate and mouse rod synaptic terminals. Invest Ophthalmol Vis Sci 63:11.

Vardi N, Duvoisin R, Wu G, Sterling P (2000) Localization of mGluR6 to dendrites of ON bipolar cells in primate retina. J Comp Neurol 423:402–412.

Yang X-L (2004) Characterization of receptors for glutamate and GABA in retinal neurons. Prog Neurobiol 73:127–150.

Yee CW, Ivanova E, Toychiev AH, Willis DE, Sagdullaev BT (2018) Atypical expression and activation of GluN2A and GluN2B-containing NMDA receptors at ganglion cells during retinal degeneration. Neuroscience 393:61–72.

Zampighi GA, Schietroma C, Zampighi LM, Woodruff M, Wright EM, Brecha NC (2011) Conical tomography of a ribbon synapse: structural evidence for vesicle fusion. PLoS One 6:e16944.